RESEARCH ARTICLE

NMR IN BIOMEDICINE WILEY

Realistic head-shaped phantom with brain-mimicking metabolites for 7 T spectroscopy and spectroscopic imaging

Ghil Jona[1] | Edna Furman-Haran[1,2] | Rita Schmidt[2,3] 🄳

[1]Life Sciences Core Facilities, Weizmann Institute of Science, Rehovot, Israel

[2]The Azrieli National Institute for Human Brain Imaging and Research, Weizmann Institute of Science, Rehovot, Israel

[3]Neurobiology Department, Weizmann Institute of Science, Rehovot, Israel

Correspondence
Dr. Rita Schmidt, The Azrieli National Institute for Human Brain Imaging and Research, Weizmann Institute of Science, Rehovot, Israel
Email: rita.schmidt@weizmann.ac.il

Purpose: Moving to ultra-high fields (≥7 T), the inhomogeneity of both RF (B_1) and static (B_0) magnetic fields increases, which further motivates us to design a realistic head-shaped phantom, especially for spectroscopic imaging. Such phantoms provide images similar to the human brain and serve as a reliable tool for developing and examining methods in MRI. This study aims to develop and characterize a realistic head-shaped phantom filled with brain-mimicking metabolites for MRS and magnetic resonance spectroscopic imaging in a 7 T MRI scanner.

Methods: A 3D head-shaped container with three sections—mimicking brain, muscle and precranial lipid—was constructed. The phantom was designed to provide robustness to heating, mechanical damage and leakage, with easy refilling. The head's shape and the agarose mixture were optimized to provide B_0 and B_1 distributions and T_1/T_2 relaxation values similar to those of human brain. Eight brain-tissue-mimicking metabolites were included for spectroscopy. The phantom was evaluated for localized spectroscopy, fast spectroscopic imaging and fat suppression.

Results: The B_0 and B_1 maps showed distribution similar to that of human brain, with increased B_0 inhomogeneity near the nasal and ear areas and reduced B_1 in the temporal lobe and brain stem regions, as expected in vivo. The metabolites' concentrations were verified by single-voxel spectroscopy, showing an average deviation of 11%. Fast spectroscopic imaging and imaging with fat suppression were demonstrated.

Conclusion: A 3D head-shaped phantom for human brain imaging and spectroscopic imaging in 7 T MRI was demonstrated, making it a realistic phantom for methodology development at 7 T.

KEYWORDS
3D-printed head-shaped phantom, brain-mimicking phantom, spectroscopic imaging, ultra-high field MRI

1 | INTRODUCTION

Phantoms designed to mimic specific in vivo features are essential in medical imaging, and are employed in many MRI applications.[1] The main purposes of phantoms in MRI include validation of specific scan methodologies and assistance in the preparation of scan protocols for human procedures. The former usage includes phantoms designed to reliably estimate specific tissue properties,[2–4] such as T_1, T_2, diffusion. The latter purpose is motivated by the limited time of actual human MRI scanning, which requires methodical provisions of the scan protocols to be completed beforehand. In daily scan preparations, simple phantoms, such as liquid-filled spherical or cylindrical containers, can suffice. However, the similarity between the images scanned in a phantom and in vivo can be crucial, for example, when a static magnetic field (B_0) distribution similar to that present in vivo is required.[5,6] For brain imaging, shaped phantoms are designed to mimic the B_0 distribution marking the susceptibility effects near nasal and ear areas.[7,8] When moving to ultra-high fields (≥7 T), the inhomogeneity of both the RF magnetic field (B_1) and B_0 increases, motivating further the design of a realistic head-shaped phantom,[9] especially for spectroscopic imaging. Central aspects of mimicking in vivo features include increased B_0 inhomogeneity (based on susceptibility effects, such as air cavities), B_1 inhomogeneous distribution, local specific absorption rate (SAR) hot-spots with potential local heating (due to the electrical tissue's properties), T_1/T_2 properties and other MRI properties that are scan dependent.

Recent studies highlight the increased interest and high potential of three-dimensional (3D) printed shaped phantoms for practical usage in MRI.[10,11] Such designs can include several compartments and simulate in vivo structures. A 3D head-shaped phantom representing in vivo brain B_0 distribution was demonstrated in 7 T MRI.[7] Recent studies have demonstrated 3D head-shaped phantoms for temperature measurements at 7 T MRI,[12] simulating potential heating during in vivo scanning. In addition, a 3D head-shaped phantom was produced to examine geometry accuracy and distortions at 3 T and 7 T scanners.[13] Other studies have examined the use of agarose filling[12,14] for temperature measurements as well as for better simulation of the in vivo T_2/T_2^* relaxation times. In this study, we aimed to combine the benefits of the above advancements.

Of special concern, when it comes to 7 T MRI, is the increased B_1 inhomogeneity, due to higher RF and the tissue's electrical properties. Several methods have introduced phantom designs with a B_1 distribution similar to human for 7 T MRI, controlling the electrical conductivity and permittivity. Previous studies showed that controlling the electrical conductivity can be achieved by adjusting the amount of NaCl, and shortening the T_1 by modifying the $NiCl_2$ concentration.[14] Reducing the relative electrical permittivity has been demonstrated using sucrose or polyvinylpyrrolidone (PVP) mixed with water.[15,16] Since these materials can also affect the ^{1}H spectrum, we found the implementation based on References 7 and 14—changing only the conductivity to match the brain tissue—more suitable for our study.

^{1}H MRS and magnetic resonance spectroscopic imaging (MRSI) are increasingly used in clinical research to characterize brain metabolism, particularly at ultra-high field (≥7 T), and benefit from increased signal to noise ratio and a gain in spectral resolution.[17–21] This field includes functional - research,[22,23] clinical assessment of neurological disorders[24,25] and pathology.[26] However, the increased B_0 and B_1 inhomogeneity and higher SAR give rise to technical challenges before robust clinical applications. The MRS and MRSI pulse sequences require a set of RF pulses, including water and lipid suppression, as well as a set of refocusing pulses, which are prone to both B_1 and B_0 inhomogeneity. A 3D head-shaped phantom with brain-mimicking metabolites can assist in establishing optimal parameters of the scans as well as optimal choice of the pulse sequence and its pulses.

We here report on the development and characterization of a realistic head-shaped phantom with brain-mimicking metabolites for spectroscopy and spectroscopic imaging in 7 T MRI. The quality of spectroscopic imaging prominently depends on the local B_0 inhomogeneity. For this purpose, a 3D head-shaped container and agar-based suspension were planned and implemented. The design objectives include B_0 and B_1 distribution similar to that of human brain, representing in vivo T_1/T_2 values, a brain-mimicking metabolite composition and lipid compartment. The phantom was examined for localized spectroscopy, fast spectroscopic imaging and fat suppression in 7 T MRI.

2 | METHODS

2.1 | 3D printed head-shaped container assembly

The 3D CAD files for the head-shaped container in this work were based on the Martinos Center's phantom design[7,12,27]—MGH Angel 001. Its inner structure was specifically designed to improve the resemblance to human brain B_0 inhomogeneity. The 3D printed parts (printed by Laser Modeling, Ness Ziona, Israel) included two inner skull-shaped halves and two outer head-shaped halves. Once printed, the inner and then the outer halves were glued together. Several changes, discussed below, were introduced to improve the use in practice, increasing robustness to heating, mechanical damage and leakage, with improved design for easy refilling.

2.1.1 | Improved robustness

Nylon powder was chosen as the printing material over commonly used ABS plastic, since it provides higher mechanical strength and temperature resistance (stable at 195 °C). In addition, it has low water absorption and, therefore, does not require any additional steps for waterproofing.

Cyanoacrylate was used to glue the halves. The glue was tested for temperature resistance up to 100 °C. Note that there may be leakage if the phantom content is reheated above 100 °C or for a long period of time.

2.1.2 | Refilling

Compared with the original design, which used sealed caps, our design includes three screw caps for easy refill (see Figure 1). One cap is positioned at the top of the inner space (the brain compartment) and two additional caps are positioned in the outer space (one on the top, the other at the bottom). The two caps of the outer space are useful for controlled filling and draining.

2.1.3 | CAD files

The files with STL format for the designed head-shaped container can be found in GitHub[28] (under the name "Shimi"). Note that, although Shimi is successfully used for 7 T MRI imaging and spectroscopy, as demonstrated in Section 3, when used with a Nova coil it completely occupies the available space. To add flexibility to the setup, we prepared an additional 3D head container, named "Gadi," that was 2% smaller than the original size and in which about 2 mm from the outer front and back parts was manually removed (see Supporting Information Figure S1). In Gadi, only the brain compartment was filled, which can be useful to simulate and examine scanning "brain" only (see Supporting Information Figure S2).
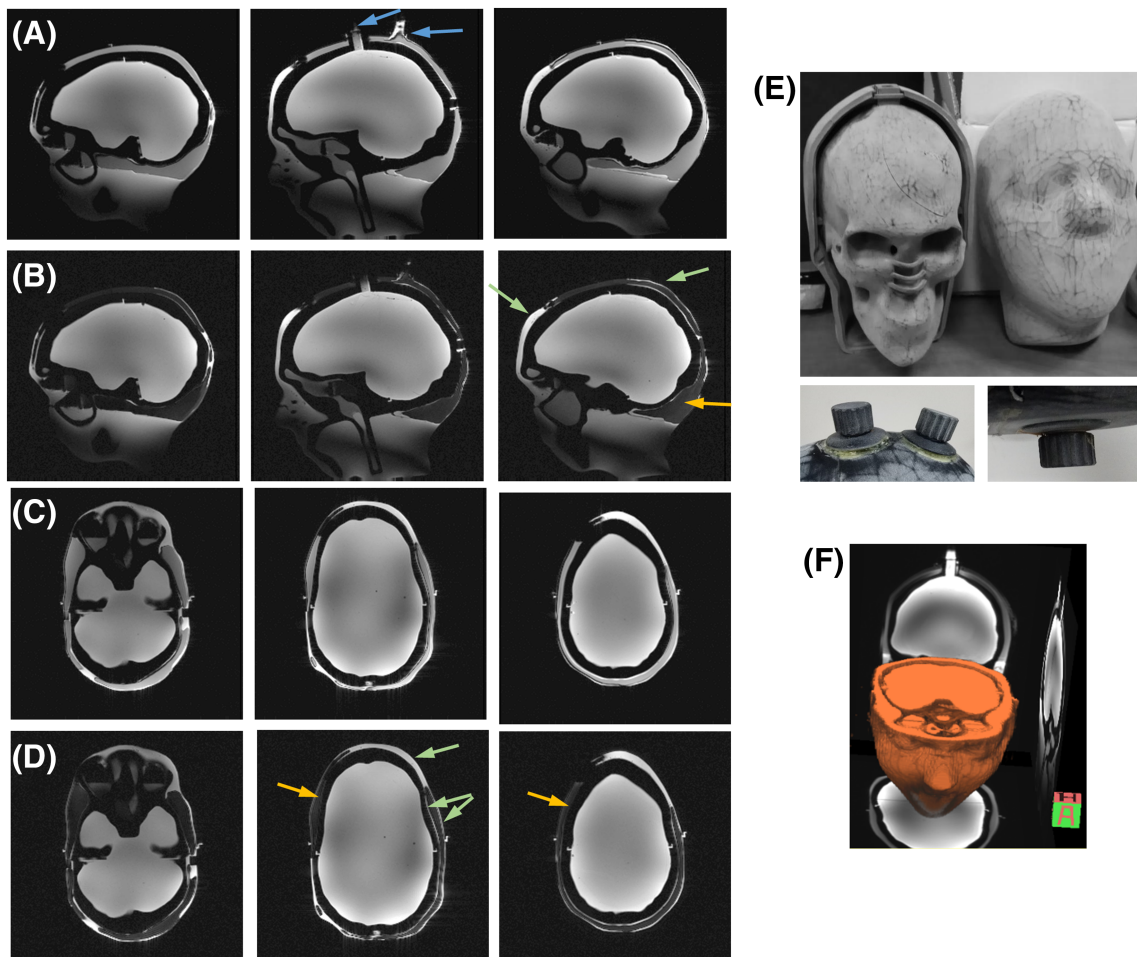

FIGURE 1   Representative images of the 3D head-shaped phantom. A-D, Sagittal and axial GRE images of the phantom acquired without fat suppression (A, C) and with fat suppression (B, D). The blue arrows show the opening for filling. The green arrows show the thin layer generated around the lipid layer as well as the locally thicker layer of the "muscle," which improve the phantom's resemblance to a realistic brain, and the orange arrows show the location of the "lipid" layer. E, Photographs of the 3D printed structure (inner and outer halves), two screw caps (left) and bottom cap (right). F, 3D rendering of phantom images

2.2 | Phantom mixture considerations and preparation

The phantom was designed to include three sub-sections—mimicking brain, muscle and lipid tissues. The inner compartment was filled with a brain-mimicking mixture. The outer compartment was divided into two sections—the bottom one mimics muscle tissue, and the top one the lipid precranial layer in proximity to the skull. In the current implementation, the muscle and brain sections were both filled with the same mixture, since the focus of our study was on mimicking the brain tissue for MRSI applications. However, for optimization of the muscle tissue, agarose and gadolinium concentration can be adjusted to fit the muscle properties as described, for example, in Reference 12.

To mimic the exact B_1 distribution, one needs to simulate both the electrical conductivity and permittivity of a human brain. However, the materials commonly used to decrease the electrical permittivity are sucrose, PVP or alcohols. The first two can introduce a more complicated shaped-phantom filling procedure, due to their increased adhesiveness. Filling with these mixtures has a high potential to generate air bubbles. All three materials may also introduce undesired ^{1}H peaks in the spectrum. Therefore, in this study we used NaCl (5.5 g/L), as in Reference 14, to exhibit a B_1 distribution comparable to human in 7 T MRI. The relative permittivity (ε_r) of 79 and conductivity (σ) of 0.6 S/m was measured using a dielectric kit (DAK-12, SPEAG, Zurich, Switzerland). We used 0.1 mM gadopentetate dimeglumine (GdDTPA) to simulate a T_1 similar to that of the human brain's white matter. It is important to note that our examination of $NiCl_2$ (as in Reference 14) for this purpose found it to significantly reduce the glutamate and N-acetyl aspartate (NAA) multiplet peaks of the spectrum (not shown). Agarose (2.5%) was used to provide a T_2 similar to that of human brain white matter. Eight brain-mimicking metabolites were added to the phantom. The brain-mimicking metabolites for spectroscopic peaks, based on Reference 29, comprised the following solution: 10 mM L-glutamic acid (Glu), 10 mM creatine (Cr) and phospho-creatine (PCr) (together Cr + PCr), 8 mM myo-inositol (mI), 2 mM gamma-aminobutyric acid (GABA), 2 mM choline chloride (Cho), 5 mM sodium lactate (Lac) and 12.5 mM NAA. Potassium dihydrogen orthophosphate was used as a buffer to achieve a pH of about 7 (typically titrated using about 2.13 g/L sodium hydroxide pellets). Sodium azide (0.27 g/L) can be added to prevent bacterial growth (it was not added in the current implementation, but will be added in the future to prolong the lifetime of the phantom and to prevent decomposition of metabolites into other by-products). Peanut oil was used in the outer compartment to mimic lipid tissue.[30]

The preparation was based on the protocol for the fBIRN stability phantom[14] protocol with some modifications. Briefly, we prepared two concentrated stock solutions: one containing a 2× mixture of the above metabolites, and the second containing a 2× potassium dihydrogen orthophosphate buffer titrated to pH 7.0 with NaOH pellets. Equal volumes of each solution were mixed, and the pH was corrected to 7.0. Next, the appropriate amount of agarose was added, and the solution was subjected to a 20 min autoclaving cycle. Finally, the solution was placed on a magnetic stirrer for 15-20 min to remove trapped air bubbles and then supplemented with the appropriate amount of GdDTPA (to 0.1 mM), before pouring.

2.3 | Phantom filling procedure

The filling procedure was especially optimized to reduce bubble formation. The described above recipe was prepared. The head-shaped container was preliminarily heated to 100 °C. The inner compartment was gradually filled (estimated volume of 1.4 L), followed by the gradual filling of the bottom section of the outer compartment (estimated volume of 1.6 L). Next, the phantom was gently rolled to generate a thin layer on the internal walls of the container to mimic the skin/muscle layer in the outer space adjacent to the lipid tissue (see green arrows in Figure 1). The phantom was then gradually cooled in a preheated oven overnight. The preliminary heating of the phantom container and a gradual cooling help to eliminate ruptures that otherwise occur due to a non-uniform cooling of the agarose mixture. Peanut oil (∼0.45 L) was added to fill the upper section of the outer compartment to mimic the lipid layer.

2.4 | Electromagnetic simulations

3D electromagnetic simulations of the B_1 field distribution in the designed phantom were performed using FIT (finite integration technique) software (CST Studio, Dassault Systemes, Darmstadt, Germany). The setup included an eight-rung ideal birdcage coil (inner diameter 30 cm) loaded with a model of the phantom—based on an MRI scan with isotropic 1 mm voxels. The simulations examined the B_1 distribution for three different sets of electrical properties for the phantom: (a) ε_r = 51, σ = 0.6 S/m—equal to the previously established brain target values[12]; (b) ε_r = 78, σ = 0.6 S/m—increasing only the conductivity[7], while leaving the permittivity as in water (as was implemented in this study); (c) ε_r = 78, σ = 0.1 S/m—electrical properties as in water, but with slightly increased conductivity (in water ε_r = 78 and σ = 0 S/m).

2.5 | MR acquisition

The experiments were performed on a 7 T MRI system (Terra, Siemens, Erlangen) using a commercial 1Tx/32Rx head coil (Nova Medical, Wilmington, MA).

2.5.1 | Final phantom configuration imaging

Scans to examine the phantom's final configuration were performed with a gradient-echo (GRE) sequence, with and without fat suppression. The scan parameters were T_R/T_E 367/2.8 ms, FOV 256 × 256 × 240 mm^3, in-plane resolution 1 × 1 mm^2, slice thickness 2 mm, BW 890 Hz/Px.

2.5.2 | B_0, B_1 and reference amplitude comparison

The B_0, B_1 and reference amplitude were examined in comparison to the human imaging with a set of Siemens product imaging protocols (GRE-field-mapping, b$_1$-tfl and transmitter amplitude adjustment, respectively). The reference amplitude is an output of the transmitter amplitude adjustment used later on to calibrate the RF pulse voltage. The B_0 mapping scan parameters were $T_R/T_{E1}/T_{E2}$ 255/3.06/4.08 ms, FOV 256 × 216 × 100 mm^3, in-plane resolution 2 × 2 mm^2, slice thickness 2.5 mm, BW 990 Hz/Px. The B_1 mapping scan parameters were T_R/T_E 7060/30 ms, FOV 256 × 256 × 96 mm^3, in-plane resolution 2 × 2 mm^2, slice thickness 4 mm. B_0 and B_1 maps were also collected in human volunteers, who provided written informed consent, following procedures approved by the Internal Review Board of the Wolfson Medical Center (Holon, Israel). Representative maps from the human imaging were selected.

2.5.3 | T_1 and T_2 relaxation measurements

T_1 and T_2 relaxation values were measured with Siemens product turbo gradient spin-echo (TGSE) and multi-contrast spin-echo (SE-MC) sequences and evaluated with single-component exponential fitting. The T_1 scan parameters were T_R/T_E 6000/40 ms, FOV 220 × 220 mm^2, in-plane resolution 2.75 × 2.75 mm^2, slice thickness 5 mm, turbo-factor 7, axial orientation. T_1 mapping included 15 inversion time (T_I) points in the range of 100-1400 ms. Oil properties were estimated in a separate scan with a peanut oil sample in a 50 mL tube, including 15 T_I points in the range of 50-1400 ms. The T_2 mapping scan parameters were T_R 4000 ms, FOV 220 × 220 mm^2, in-plane resolution 0.5 × 1.0 mm^2, slice thickness 5 mm, axial orientation, 32 echo time (T_E) points covering a T_E range of 14-450 ms. The estimation of the T_1/T_2 relaxation times of the metabolites was based on single-voxel spectroscopy (PRESS) with a 20 × 20 × 20 mm^3 voxel at the center of the "brain." The T_2 relaxation times of the metabolites were estimated by varying T_E (keeping T_R constant). The T_1 relaxation times were estimated from a series of steady-state scans, each with a different T_R (keeping T_E constant). The scan parameters for T_2 estimation were T_R 4000 ms, spectral width (SW) 4 kHz, 32 averages, repeated for 20 T_E values in the range 40-1700 ms. The scan parameters for T_1 estimation were T_E 30 ms, SW 4 kHz, 64 averages, repeated with 13 T_R values in the range 450-4000 ms.

2.5.4 | Single-voxel spectroscopy and spectroscopic imaging

Single-voxel spectroscopy (PRESS) at the center of the "brain" was performed with an SVS-SE Siemens product sequence. The scan parameters were T_R/T_E 4000/30 ms, voxel dimensions 20 × 20 × 20 mm^3, SW 4 kHz, 32 averages. Spectra were acquired with and without water suppression for reference. The spectrum was apodized with an exponential filter (e$^{-t/APO}$, APO = 100 ms)[31] and fitted in LCModel44 (v6.3)[32] using basis sets provided by LCModel. LCModel fitting parameters that were specifically tuned for optimal results included adjusting of the lower and upper limits of the ppm range for the analysis, to 1.0 ppm and 4.1 ppm respectively. For comparison, a single-voxel spectroscopy scan was also acquired in the white matter region of a human brain, applying the same scan parameters.

Spectroscopic imaging was performed with a custom written spin-echo (SE) EPSI sequence. The water/oil EPSI imaging was performed with the following scan parameters: T_R/T_E 1550/18 ms, FOV 260 × 260 mm^2, in-plane resolution 6.5 × 4.0 mm^2, slice thickness 10 mm, 11 axial slices, echo spacing (esp) 0.4 ms, SW 1250 Hz, total scan duration 1 min 40 seconds. Metabolite EPSI imaging was performed with an in-house 180 ms optimized VAPOR-like model consisting of six frequency-selective pulses.[33] Two scans were performed with two sets of SW and spatial resolution. The Set 1 scan parameters were T_R/T_E 2000/18 ms, FOV 300 × 300 mm^2, in-plane resolution 4.3 × 4.3 mm^2 (70 × 70 pixels), slice thickness 20 mm, single slice, esp 0.52 ms, SW 960 Hz, total scan duration 2 min 20 s. The Set 2 scan parameters were T_R/T_E 2000/18 ms, FOV 260 ×

260 mm^2, in-plane resolution 8.7 × 4.0 mm^2 (30 × 64 pixels), slice thickness 20 mm, single slice, esp 0.33 ms, SW 1500 Hz, total scan duration 2 min 8 s.

When reconstructing the spectroscopic image, we used odd echoes only to avoid ghosting in the spectrum. A 2D Hamming filter was used to reduce the point spread function (PSF) side bands. The contribution of the receive channels to the acquired signal was evaluated using a water reference scan, with the final signal estimated based on Reference 34. The final spectrum results show a real component spectrum after zero- and first-order phase corrections for 5 × 5 voxels. Images for specific peaks were generated using straightforward integration around the peak.

To compare the intensity distribution measured in the EPSI images, three additional acquisitions were performed with the following sequences: GRE (which includes only an excitation pulse), SE (which includes an excitation pulse and a refocusing pulse as in EPSI) and MP2RAGE (which combines two GRE readouts acquired with two inversion times, T_{I1} and T_{I2}, into a final image such that the B_1 distribution is canceled out). The common scan parameters of the scans were FOV 260 × 260 mm^2, in-plane resolution 1 × 1 mm^2, slice thickness 5 mm. Specific scan parameters were GRE scan—T_R/T_E 137/3 ms, flip angle 25°; SE scan—T_R/T_E 1000/7.8 ms; MP2RAGE—T_R/T_E 3000/3 ms, flip angle 4°, T_{I1}/T_{I2} 1000/2000 ms.

3 | RESULTS

Phantom images of the final configuration are demonstrated in Figure 1. The images show no significant bubble content, and a structure similar to that of the human brain. The images with and without applied fat suppression emphasize the precranial "lipid" layer and the surrounding thin layer generated to mimic skin/muscle in the outer space adjacent to the lipid layer.

Figure 2 shows simulations of the B_1 field distribution in a human brain for three sets of electrical properties. In Figure 2A the electrical properties best match those of an actual brain and give the expected central brightening. In Figure 2B, with only the conductivity being similar to that in vivo, the width of the central brightening is smaller and the signal drop is larger. In the last case, Figure 2C, the electrical properties are close to those of water and a severe signal drop is observed. Finally, for each case, a histogram of the B_1 values for all voxels in the brain is shown in Figure 2D. Each histogram can be summarized by the coefficient of variation (CV—standard deviation (SD) divided by the average inside the "brain" compartment) for that case—A, CV = 36.5% (ε_r = 51, σ = 0.6 S/m), B, CV = 41% (ε_r = 78, σ = 0.6 S/m); C, CV = 58% (ε_r = 78, σ = 0.1 S/m). Note that although lower intensities are reached in case B compared with case A—mimicking only brain conductivity compared with mimicking both conductivity and permittivity—the CVs of the two differ by only 4.5%. Considering that the main objective of this study is to mimic the brain metabolite behavior in spectroscopic imaging, case B can be used to achieve B_1 distribution similar to that of the real brain and to mimic a brain-like ^{1}H spectrum.

The comparison of human and phantom B_0 maps after optimal shimming of the brain volume is summarized in Figure 3, and the detailed B_0 maps are included in Supporting Information Figure S3. Figure S3 also shows another set of human brain B_0 maps to indicate a potential range of distributions due to the different brain sizes and local deviations. Maximal absolute projections of the B_0 deviations ($\max_z(|\Delta B_{0(x,y,z)}|)$) in two directions were calculated (the axial plane shows projections in the slice direction and the sagittal plane shows projections in the left/right direction). Images of the maximal deviation projection emphasize the main inhomogeneous areas in the comparison—clearly demonstrating high values near nasal, eye and ear regions, similar to human brain results. Note that an undesired asymmetry was observed in the phantom B_0 map, with high values on the left-hand side of the axial image, which is most likely a result of some imperfections in the 3D printing of the nose-mimicking structure.[7] The range of the maximal deviations in the human and in the phantom reached 250 Hz (similar to Reference 35) and 200 Hz, respectively. Histograms of the B_0 maps in the brain volume were plotted and the frequency linewidth at half maximum (FWHM) was estimated, resulting in a linewidth of 17 Hz in a human volunteer sample and 13 Hz in the phantom.

A comparison of human and phantom B_1 maps is shown in Figure 4, summarized in central sagittal and axial scans (Supporting information Figure S4 includes higher coverage of the B_1 maps). The human CV was 37% and 28% for sagittal and axial scans, respectively, and the phantom CV was 23% and 18%, respectively. The whole brain CV was 33% for human and 31% for phantom. The slightly higher CV in the human scan (and not lower as expected from the simulations) can be explained by the lower SNR in the higher B_0 inhomogeneous areas. Figure 4C shows the 1D profiles in the center of each plane, normalized to the maximum of the central peak. As expected from the simulation, the width of the central brightening area in the phantom is smaller than in human, due to the higher permittivity in the phantom. In addition, the reference amplitudes, used for RF pulse calibrations (based on a 1 ms 180° hard pulse) of the human volunteer and the phantom were estimated as 240 V and 216 V, respectively. This predicts about 20% lower SAR percentage when planning scans in the phantom compared with in vivo scanning.

T_1 and T_2 relaxation times of the "brain" compartment were estimated in the central area (144 pixels) of the central slice as 1160 ± 35 ms and 57 ± 2 ms, respectively; those of the "lipid" compartment were estimated as 426 ± 1 ms and 145 ± 1 ms, respectively. T_1/T_2 relaxation times of the metabolites are summarized in Table 2.

FIGURE 2 A-C, Electromagnetic simulations—central sagittal and axial planes of the B_1 field for $\varepsilon_r = 51$, $\sigma = 0.6$ S/m (A), $\varepsilon_r = 78$, $\sigma = 0.6$ S/m (B) and $\varepsilon_r = 78$, $\sigma = 0.1$ S/m (C). Each map is scaled from 0 to maximum. D, Histogram of the B_1 distribution in the brain for each case. The Y-axis shows the fraction of the total number of voxels

(A) $\varepsilon_r=51$, $\sigma=0.6$ S/m, CV=36.5% μT/√w

(B) $\varepsilon_r=78$, $\sigma=0.6$ S/m, CV=41.0%

(C) $\varepsilon_r=78$, $\sigma=0.1$ S/m, CV=58.0.0%

(D) Histogram of the B_1 distribution

- $\varepsilon_r=51$, $\sigma=0.6$ S/m
- $\varepsilon_r=78$, $\sigma=0.6$ S/m
- $\varepsilon_r=78$, $\sigma=0.1$ S/m

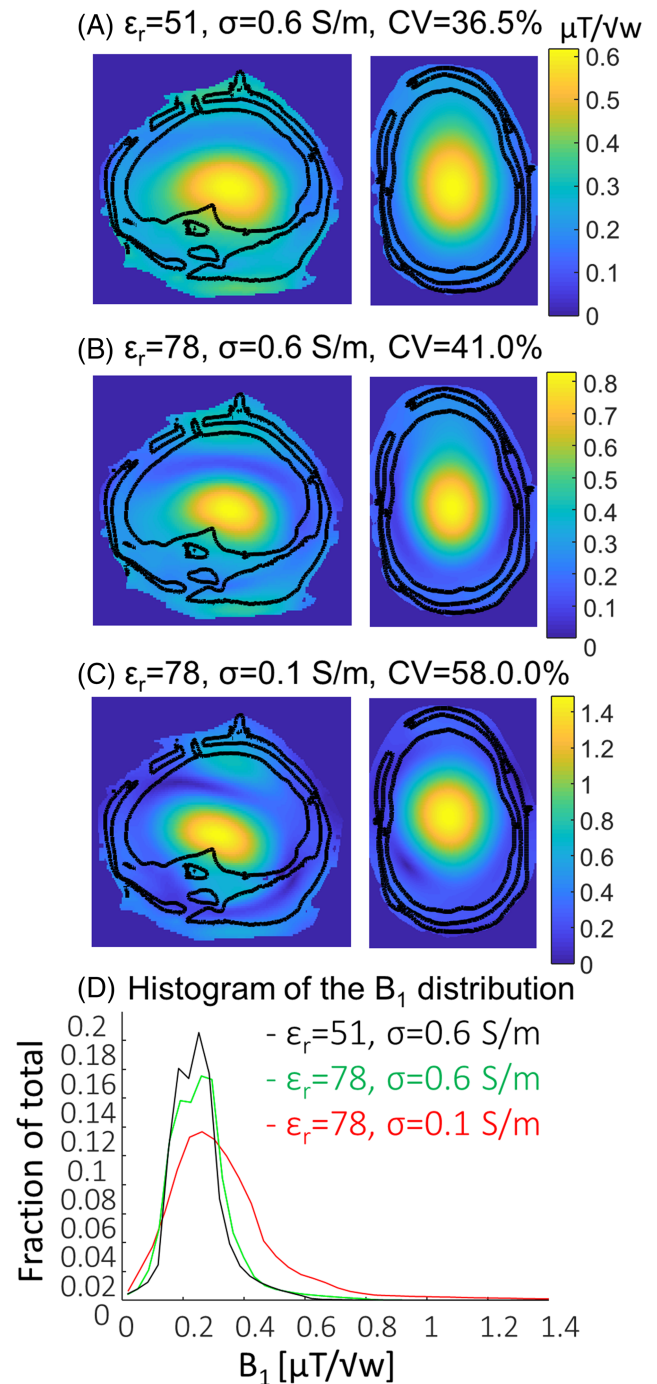Fraction of total

B_1 [μT/√w]

Figure 5 shows the single-voxel spectrum in the phantom and in a human brain. The LCModel fitting and measured concentrations were estimated for the main peaks and are summarized in Table 1, with an estimated average deviation from the actual values of 11%. The average SD of the LCModel fitting (excluding GABA, since usually it requires a dedicated pulse sequence) was 4.8% for phantom and 3.6% for human. Figures 6 and 7 show spectroscopic imaging performed with EPSI sequences. Figure 6 shows water/oil images and representative water/oil spectra. Due to the high water signal and B_0 inhomogeneity, some residual water signal exists in the oil images. Figure 7 compares two acquired EPSI scans. Set 1 targeted high spatial resolution, which required reduction of the SW. The limited SW ($\sim$1000 Hz) results in significant baseline in both spectrum edges due to the water peak (Figure 7C). Set 2 acquired lower spatial resolution with large enough SW for 7 T ^{1}H spectra. The figure shows the water magnitude images and the NAA and Cr images as well as representative spectra in voxels moving from the center of the phantom to the edge. The average CV of the metabolite images in Figure 7 is 28% ± 6%, the CV in the SE image is 27% and that in MP2RAGE is 6%. The intensity variations are localized in the B_1 inhomogeneous areas, as shown in Figure 4. This variation can be reduced if adiabatic pulses are used.
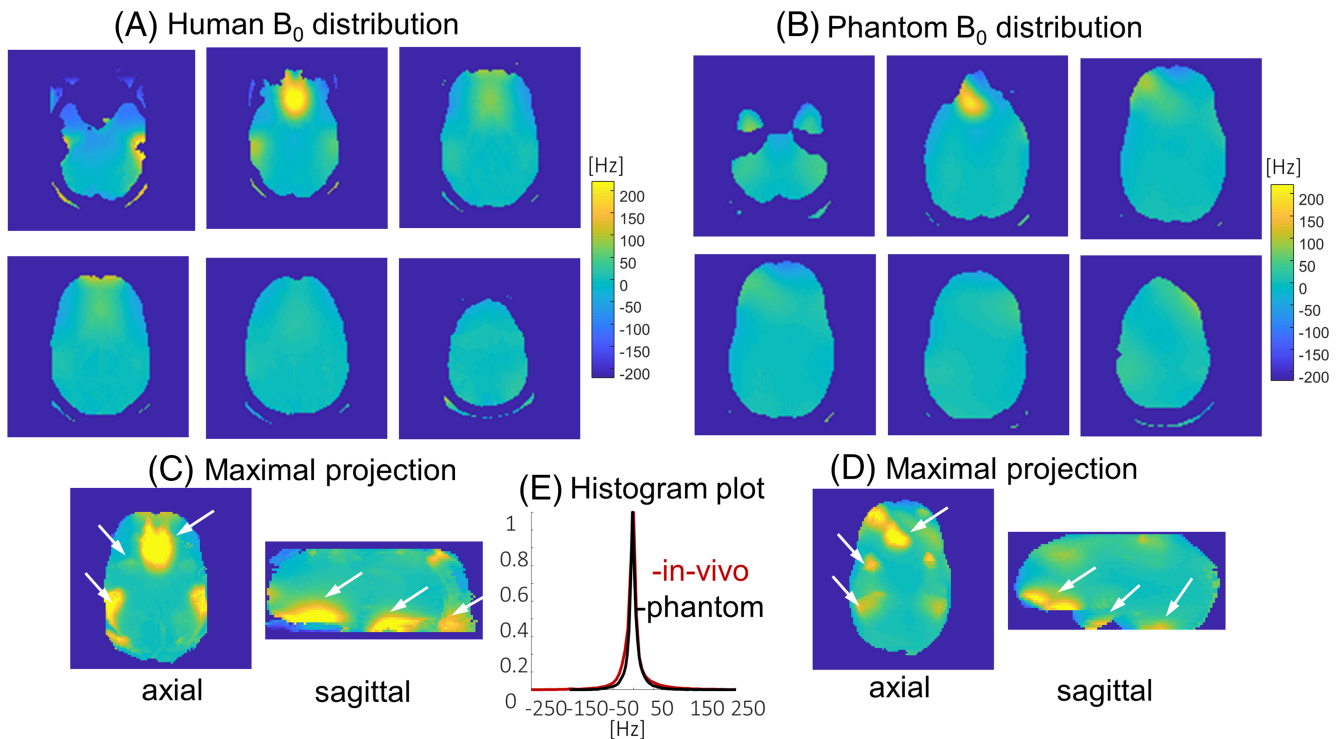
FIGURE 3 B_0 distribution comparison. A, B, Six axial representative slices of the human (A) and phantom (B) brain B_0 distribution. C, D, Maximal absolute projection in the axial and sagittal planes for human (C) and phantom (D) brain. E, Histogram plot comparison (FWHM = 17 Hz and 13 Hz for human and phantom, respectively). Arrows point to the main inhomogeneous areas

4 | DISCUSSION

3D printed phantoms can serve as a reliable tool for the development of new MR technologies and as a practical and easy solution to improve the quality of human scanning by examining the scan protocols before the actual scanning. Such phantoms are of high interest for 7 T imaging and are even more essential for spectroscopic imaging, where B_1 inhomogeneity affects the quality of water and lipid suppression pulses, and B_0 inhomogeneity influences both water and lipid contamination and scan protocols, such as resolution and SW, requiring proper optimization. In this study, we have designed a 3D printed phantom based on Reference 17 with improved robustness to heating, mechanical damage and leakage. The design incorporated the addition of screw caps to improve refilling. It further included optimization of the "brain" composition, and of the preparation and the filling procedures to improve the content homogeneity and to reduce air bubble formation. The described procedure significantly reduces the tendency for large bubbles to get trapped in the bottom part of the skull and near the opening. The long heating and gradual cooling was found to be essential to avoid the formation of a rupture near the opening, drawn to the center of the "brain" (not shown).

3D electromagnetic simulations were performed to examine the compromise between better matching of the brain electrical properties (achieving a higher degree of similarity in B_1) and the objective of mimicking well the ^{1}H spectra of brain metabolites. The simulation with ε_r = 78, σ = 0.6 S/m (the values implemented in the phantom) showed a B_1 CV which is only 4.5% higher than with in vivo electrical properties, corroborating our implementation. The B_0 and B_1 distributions measured in the phantom "brain" were in good agreement with human brain distribution, which is an important feature for the practical usage of the phantom. The maximal deviations of the B_0 maps appeared near the nasal, eye and ear areas, as expected due to the increased susceptibility caused by the air/tissue interface (see the arrows in Figure 2). The imperfections in the 3D printing of the mimicked nose structure could have caused the local asymmetry in the B_0 map observed in the phantom. To further mimic the local intra-voxel T_2^* distribution, one needs to simulate a heterogeneous head phantom, which is beyond the scope of this study. The B_1 distribution shows central brightening and an intensity drop in the temporal lobe and brain stem areas, which is similarly well represented in the phantom (see the arrows in Figure 4). However, both the B_0 estimated linewidth and the B_1 CV in the phantom were 20-25% lower compared with the human volunteer data. A similar range in the distribution can also be observed when scanning different human volunteers. The lower deviations of the phantom's B_0 distribution can be explained by inaccurately simulated air cavities compared with the human structure. The B_1 deviation from the human brain is a result of the choice not to reduce the electrical permittivity in the phantom. A compromise between some deviation from the human B_1 profile and easy phantom preparation needs to be considered. Specifically, the commonly used ingredients to reduce permittivity (PVP or sucrose) could also affect the ^{1}H spectrum, which was not desirable in this study. Another difference is the lack of shoulders in the phantom. The shoulders contribute to the electrical load and also have some effect on the B_1 distribution. However, adding shoulders to this phantom

FIGURE 4 B_1 distribution comparison. A, B, Central sagittal and axial planes of the human (A) and phantom (B) brain B_1 distribution. The maps are normalized to maximum in each case. Arrows point to areas of low B_1. C, 1D profiles over the central lines (shown as white dashed lines for sagittal and axial planes)
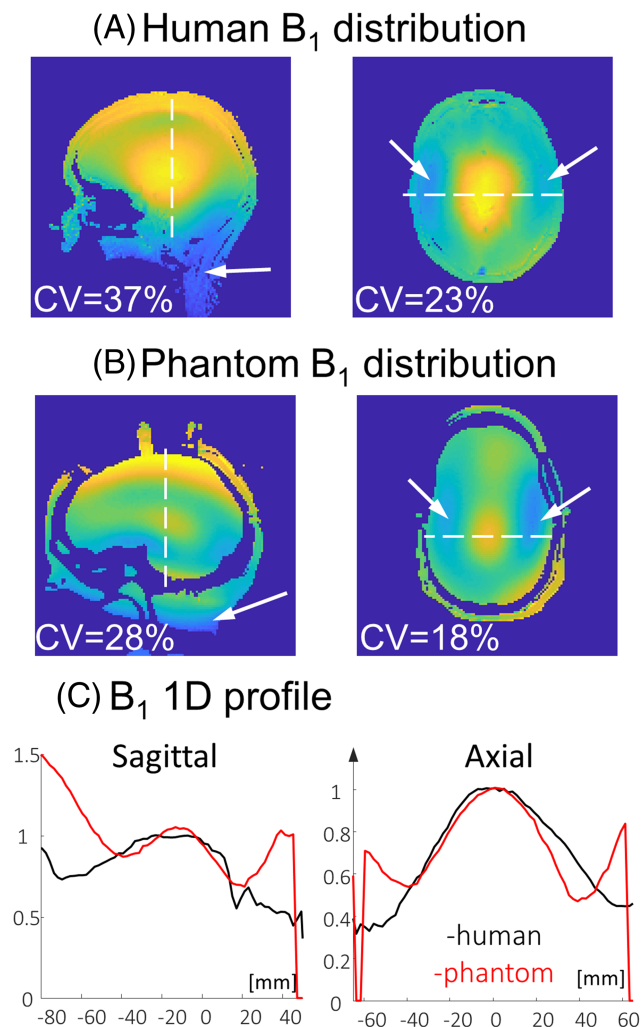

(A) Human B_1 distribution

(B) Phantom B_1 distribution

(C) B_1 1D profile

TABLE 2 Estimated T_1 and T_2 relaxation times of the metabolites in the phantom

	T_1 [ms] mean ± SD	T_2 [ms] mean ± SD
NAA	1171 ± 64	342 ± 11
Cr+PCr	1212 ± 84	202 ± 5
Cho	943 ± 73	278 ± 6
Glu	1001 ± 152	349 ± 17
ml	846 ± 87	192 ± 14
Lac	1921 ± 417	268 ± 9

makes its handling cumbersome and the weight is significantly increased. The reference amplitude showed a 10% lower amplitude in the phantom, providing a good estimate for the SAR percentage expected in human scanning.

The measured "brain" T_1 and T_2 are in good agreement with that measured in human brain white matter (T_1 ranging from 1126 to 1300 ms,[36,37] $T_2 \approx 55$ ms[38]). The oil signal was well controlled by the spectral fat suppression pulses. However, the T_1 and T_2 relaxation times are higher than the common in vivo lipid values. Further research is required to better choose the oil used to mimic the "lipid" layer, if inversion recovery pulses are of interest. Further development can include the implementation of a solid lipid layer, which can better represent in vivo lipid. The "muscle" compartment was not optimized in this study. The T_1/T_2 values of the metabolites are in the range of reported values for 7 T.[39–41]

The acquisition of single-voxel spectroscopy and MRSI was demonstrated. The average deviation of the measured concentrations of the metabolites from the actual values was 11%, with an average SD in the LCModel fit of 5% (excluding GABA). One reason for the current deviations is the narrower linewidth of the peaks in the phantom compared with in vivo. This was partially improved by applying an apodization function to the acquired signal. Another reason is the B_1 inhomogeneity inside the spectroscopy voxel, which affects the refocusing pulses in the
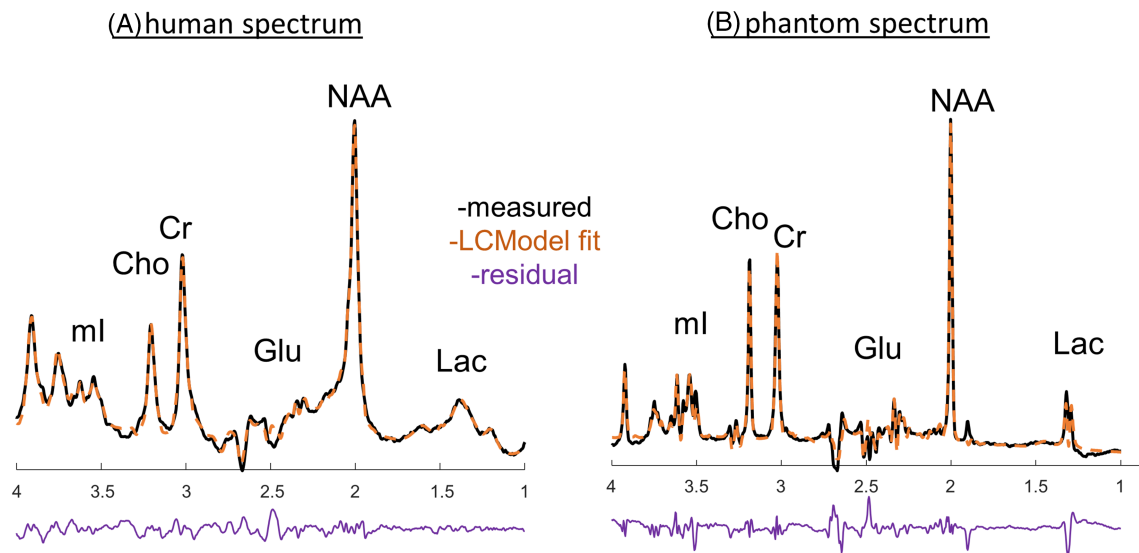
FIGURE 5 Single-voxel spectroscopy in a white matter voxel in human (A) and at the center of the phantom (B). Measured spectrum, LCModel fit and residual plots are shown

TABLE 1 Estimated concentration in phantom and human brain (white matter)

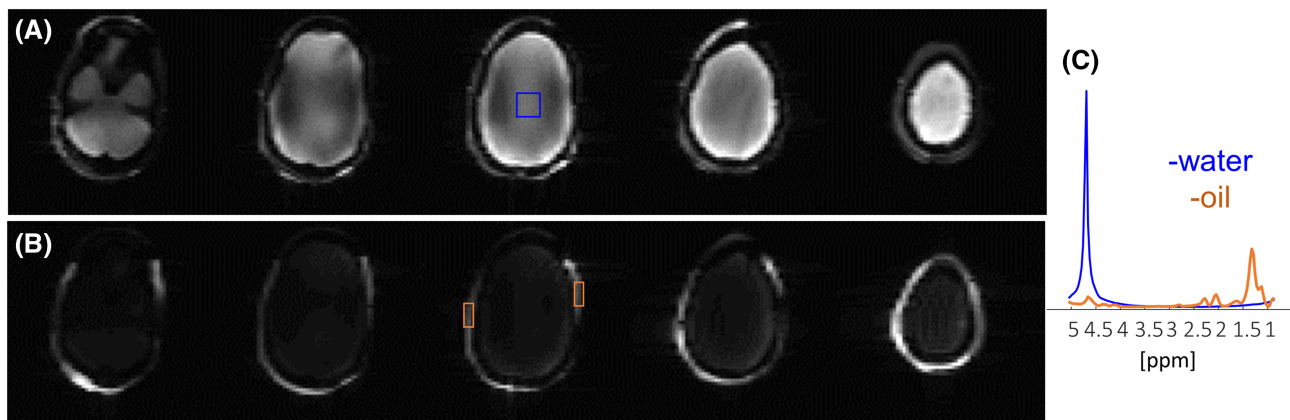|	Actual concentration in phantom [mM]	Estimated average concentration in phantom [mM]	SD [%]	Estimated average concentration in human [mM]	SD [%]
NAA	12.5	11.96	2	13.7	2
Cr+PCr	10	9.7	3	8.9	2
Cho	2	2.30	4	2.04	2
Glu	10	10.62	9	12.3	5
mI	7.5	8.36	6	5.7	3
Lac	5	3.58	6	*>100 SD due to lipid	
GABA	2	1.74	25	2.4	21

FIGURE 6 Water/fat MRSI using EPSI. A, B, Five axial slices of the water (A) and fat (B) images. C, Spectra summed for the voxels in the blue square (water) in A and in the orange rectangles (oil) in B. Scan parameters: T_R/T_E 1550/18 ms, FOV 260 × 260 mm^2, in-plane resolution 6.5 × 4.0 mm^2, slice thickness 10 mm, 11 axial slices, esp 0.4 ms, SW 1250 Hz, total scan duration 1.40 min
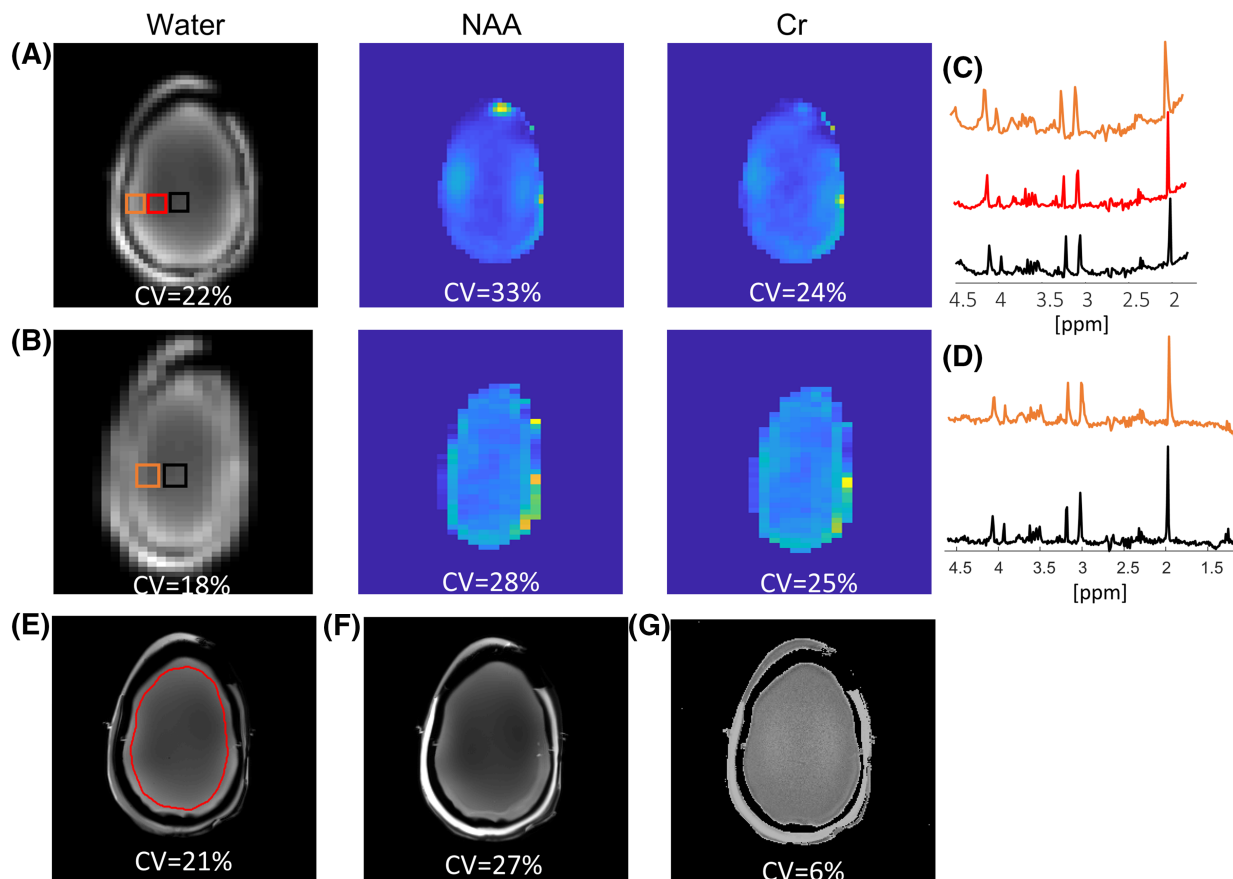
FIGURE 7   [1]H brain-mimicking metabolite MRSI using EPSI. Left to right—water magnitude, NAA and Cr images and spectrum for the regions shown on the magnitude image for Sets 1 (A, C) and 2 (B, D). The Set 1 scan parameters were T_R/T_E 2000/18 ms, FOV 300 × 300 mm^2, in-plane resolution 4.3 × 4.3 mm^2, slice thickness 20 mm, esp 0.52 ms, SW 960 Hz, total scan duration 2 min 20 s. The Set 2 scan parameters were T_R/T_E 2000/18 ms, FOV 260 × 260 mm^2, in-plane resolution 8.7 × 4.0 mm^2, slice thickness 20 mm, esp 0.33 ms, SW 1500 Hz, total scan duration 2 min 8 s. E-G, Images acquired with GRE, SE and MP2RAGE. The red overlay shows the region that was used to calculate the CV in all cases

PRESS sequence. MRS studies at 7 T suggest the use of a semi-LASER sequence[42] that utilizes adiabatic pulses, which are relatively insensitive to B_1 inhomogeneity.

The fast spectroscopic imaging in 7 T can achieve high-resolution (∼4 mm in-plane) spectral-spatial information with a high-quality spectrum. One such powerful pulse sequence is EPSI. However, EPSI is also known for its relatively limited SW, especially if only odd lines are used for analysis. To increase the SW (defined by 1/(2·esp)), one needs to reduce the number of points acquired in the readout direction, which will limit the spatial resolution. The ability to exploit such a phantom to examine EPSI parameters could be extremely valuable. In this study, we demonstrate two scans with different SWs and spatial resolutions. Set 1, with a lower SW and higher resolution, shows higher baseline deviations due to the water peak. This is improved with a higher SW; however, in this case the spatial resolution is compromised. Depending on the application of interest, one can optimize the spatial and spectral resolutions. The relatively high CV (>20%) in the EPSI images is a result of the B_1 inhomogeneity. For verification, we measured the CV in a GRE and a spin echo (SE) MRI acquisition. In a uniform phantom, the image intensity of GRE is expected to be proportional to the B_1 distribution, which will be expressed in the image CV. Adding a refocusing pulse (as in the SE and EPSI scans) will further increase the CV. The CV in the SE image was similar to that of the EPSI scans. In order to eliminate the contribution of B_1 inhomogeneity to the image distribution, we also estimated the CV in MP2RAGE[43] acquisition, which relies on two acquisitions with two inversion times that cancel out the B_1 inhomogeneity in the final image. The CV in this image was 6%.

In summary, recent studies have shown improved methods to deal with the technical challenges of 7 T, for both MRS[44] and MRSI[45]. The challenges of 7 T include SAR limitations, eg when increasing the number of pulses to support outer volume suppression and\or adiabatic pulses.[46] B_1 inhomogeneity is a further challenge, which may lead to non-optimal water and lipid suppression[47]. And of course B_0 inhomogeneity, especially close to the eyes, nose and ear regions,[48] dramatically affects the spectrum quality. The 3D phantom explored in this work should be extremely useful to investigate the robustness of an examined pulse sequence. Such a phantom can be further exploited to examine features of high interest for spectroscopic imaging in 7 T, including dynamic per-slice B_0 shimming methods[48,49] and B_1 PTx implementations. It is important to note that

this 3D-shaped phantom can also be valuable for 3 T. A dedicated study to show its benefits will be performed in the future. Figure S5 in the Supporting Information shows an example of MRI images and a spectrum acquired with this phantom at 3 T.

ORCID

Rita Schmidt 🄳 https://orcid.org/0000-0003-1580-9964

REFERENCES

1. Filippou V, Tsoumpas C. Recent advances on the development of phantoms using 3D printing for imaging with CT, MRI, PET, SPECT, and ultrasound. *Med Phys*. 2018;45(9):e740-e760.
2. Jiang Y, Ma D, Keenan KE, Stupic KF, Gulani V, Griswold MA. Repeatability of magnetic resonance fingerprinting T_1 and T_2 estimates assessed using the ISMRM/NIST MRI system phantom. *Magn Reson Med*. 2017;78(4):1452-1457.
3. Keenan KE, Ainslie M, Barker AJ, et al. Quantitative magnetic resonance imaging phantoms: a review and the need for a system phantom. *Magn Reson Med*. 2018;79(1):48-61.
4. Bane O, Hectors SJ, Wagner M, et al. Accuracy, repeatability, and interplatform reproducibility of T_1 quantification methods used for DCE-MRI: results from a multicenter phantom study. *Magn Reson Med*. 2018;79(5):2564-2575.
5. Koch KM, Hargreaves BA, Pauly KB, Chen W, Gold GE, King KF. Magnetic resonance imaging near metal implants. *J Magn Reson Imaging*. 2010;32(4): 773-787.
6. Kumar NM, Fritz B, Stern SE, Warntjes JM, Lisa Chuah YM, Fritz J. Synthetic MRI of the knee: phantom validation and comparison with conventional MRI. *Radiology*. 2018;289(2):465-477.
7. Guérin B, Stockmann JP, Baboli M, Torrado-Carvajal A, Stenger AV, Wald LL. Robust time-shifted spoke pulse design in the presence of large B0 variations with simultaneous reduction of through-plane dephasing, B1+ effects, and the specific absorption rate using parallel transmission. *Magn Reson Med*. 76(2):540-554.
8. Shmueli K, Thomas DL, Ordidge RJ. Design, construction and evaluation of an anthropomorphic head phantom with realistic susceptibility artifacts. *J Magn Reson Imaging*. 2007;26(1):202-207.
9. Yang QX, Wang J, Collins CM, et al. Phantom design method for high-field MRI human systems. *Magn Reson Med*. 2004;52(5):1016-1020.
10. Wood S, Krishnamurthy N, Santini T, et al. Design and fabrication of a realistic anthropomorphic heterogeneous head phantom for MR purposes. *PloS ONE*. 2017;12(8):e0192794.
11. Mobashsher AT, Abbosh AM. Three-dimensional human head phantom with realistic electrical properties and anatomy. *IEEE Antennas Wirel Propag Lett*. 2014;13:1401-1404.
12. Graedel NN, Polimeni JR, Guerin B, Gagoski B, Wald LL. An anatomically realistic temperature phantom for radiofrequency heating measurements. *Magn Reson Med*. 2015;73(1):442-450.
13. Peerlings J, Compter I, Janssen F. Characterizing geometrical accuracy in clinically optimised 7T and 3T magnetic resonance images for high-precision radiation treatment of brain tumours. *Phys Imaging Radiat Oncol*. 2019;9:35-42.
14. Friedman L, Glover GH. Report on a multicenter fMRI quality assurance protocol. *J Magn Reson Imaging*. 2006;23(6):827-839.
15. Duan Q, Duyn JH, Gudino N, et al. Characterization of a dielectric phantom for high-field magnetic resonance imaging applications. *Med Phys*. 2014; 41(10):1–6.
16. Brink WM, Wu Z, Webb AG. A simple head-sized phantom for realistic static and radiofrequency characterization at high fields. *Magn Reson Med*. 2018;80(4):1738-1745.
17. Tkáč I, Andersen P, Adriany G, Merkle H, Uğurbil K, Gruetter R. In vivo ^{1}H NMR spectroscopy of the human brain at 7 T. *Magn Reson Med*. 2001;46 (3):451-456.
18. Deelchand DK, Van de Moortele PF, Adriany G, et al. In vivo 1H NMR spectroscopy of the human brain at 9.4 T: initial results. *J Magn Reson*. 2010; 206(1):74-80.
19. Nassirpour S, Chang P, Henning A. High and ultra-high resolution metabolite mapping of the human brain using ^{1}H FID MRSI at 9.4 T. *NeuroImage*. 2018;168:211-221.
20. Považan M, Strasser B, Hangel G, et al. Simultaneous mapping of metabolites and individual macromolecular components via ultra-short acquisition delay ^{1}H MRSI in the brain at 7T. *Magn Reson Med*. 2018;79(3):1231-1240.
21. Chiew M, Jiang W, Burns B, et al. Density-weighted concentric rings *k*-space trajectory for ^{1}H magnetic resonance spectroscopic imaging at 7 T. *NMR Biomed*. 2018;31(1):1–14, e3838.
22. Mangia S, Tkác I, Gruetter R, et al. Sensitivity of single-voxel ^{1}H-MRS in investigating the metabolism of the activated human visual cortex at 7 T. *Magn Reson Imaging*. 2006;24(4):343-348. https://doi.org/10.1016/j.mri.2005.12.023
23. Dyke K, Pépés SE, Chen C, et al. Comparing GABA-dependent physiological measures of inhibition with proton magnetic resonance spectroscopy measurement of GABA using ultra-high-field MRI. *NeuroImage*. 2017;152:360-370.
24. Marjańska M, McCarten JR, Hodges JS, Hemmy LS, Terpstra M. Distinctive neurochemistry in Alzheimer's Disease via 7 T in vivo magnetic resonance spectroscopy. *J Alzheimer's Dis*. 2019;68(2):559-569.
25. Cheong I, Marjańska M, Deelchand DK, Eberly LE, Walk D, Öz G. Ultra-high field proton MR spectroscopy in early-stage amyotrophic lateral sclerosis. *Neurochem Res*. 2017;42(6):1833-1844.

26. Kwock L, Smith JK, Castillo M, et al. Clinical role of proton magnetic resonance spectroscopy in oncology: brain, breast, and prostate cancer. *Lancet Oncol.* 2006;7(10):859-868.

27. MGH Angel 001. *A.A. Martinos Center/Wald Group Anthropomorphic Phantom Builder's Wiki.* https://phantoms.martinos.org/MGH_Angel_001. Accessed March 24, 2015.

28. Schmidt MRI lab. *GitHub.* https://github.com/RitaSchmidt/3DRealisticHeadPhantomInMRI. Accessed April 26, 2020.

29. Schirmer T, Auer DP. On the reliability of quantitative clinical magnetic resonance spectroscopy of the human brain. *NMR Biomed.* 2000;13(1):28-36.

30. Hines CD, Yu H, Shimakawa A, McKenzie CA, Brittain JH, Reeder SB. T_1 independent, T_2^* corrected MRI with accurate spectral modeling for quantification of fat: validation in a fat-water-SPIO phantom. *J Magn Reson Imaging.* 2009;30(5):1215-1222.

31. Hájek M, Burian M, Dezortová M. Application of LCModel for quality control and quantitative in vivo ^{1}H MR spectroscopy by short echo time STEAM sequence. *Magn Reson Mater Phys Biol Med.* 2000;10(1):6-17.

32. Provencher SW. Estimation of metabolite concentrations from localized in vivo proton NMR spectra. *Magn Reson Med.* 1993;30(6):672-679.

33. Volovyk O, Tal A. Application of phase rotation to STRESS localization scheme at 3 T. *Magn Reson Med.* 2018;79(5):2481-2490.

34. Hall EL, Stephenson MC, Price D, Morris PG. Methodology for improved detection of low concentration metabolites in MRS: optimised combination of signals from multi-element coil arrays. *NeuroImage.* 2014;86:35-42.

35. Stockmann JP, Wald LL. In vivo B_0 field shimming methods for MRI at 7 T. *NeuroImage.* 2018;168:71-87.

36. Dieringer MA, Deimling M, Santoro D, et al. Rapid parametric mapping of the longitudinal relaxation time T_1 using two-dimensional variable flip angle magnetic resonance imaging at 1.5 Tesla, 3 Tesla, and 7 Tesla. *PLoS ONE.* 2014;9(3):e91318.

37. Wright PJ, Mougin OE, Totman JJ, et al. Water proton T_1 measurements in brain tissue at 7, 3, and 1.5 T using IR-EPI, IR-TSE, and MPRAGE: results and optimization. *Magma Magn Reson Mater Phys Biol Med.* 2008;21(1/2):121–130.

38. Marques JP, Norris DG. How to choose the right MR sequence for your research question at 7 T and above? *NeuroImage.* 2018;168:119-140.

39. Xin L, Schaller B, Mlynarik V, Lu H, Gruetter R. Proton T_1 relaxation times of metabolites in human occipital white and gray matter at 7 T. *Magn Reson Med.* 2013;69(4):931-936.

40. Penner J, Bartha R. Semi-LASER ^{1}H MR spectroscopy at 7 Tesla in human brain: metabolite quantification incorporating subject-specific macromolecule removal. *Magn Reson Med.* 2015;74(1):4-12.

41. Michaeli S, Garwood M, Zhu XH, et al. Proton T_2 relaxation study of water, N-acetylaspartate, and creatine in human brain using Hahn and Carr-Purcell spin echoes at 4T and 7T. *Magn Reson Med.* 2002;47(4):629-633.

42. Scheenen TW, Klomp DW, Wijnen JP, Heerschap A. Short echo time ^{1}H-MRSI of the human brain at 3T with minimal chemical shift displacement errors using adiabatic refocusing pulses. *Magn Reson Med.* 2008;59(1):1-6.

43. Marques JP, Kober T, Krueger G, van der Zwaag W, Van de Moortele PF, Gruetter R. MP2RAGE, a self bias-field corrected sequence for improved segmentation and T_1-mapping at high field. *NeuroImage.* 2010;49(2):1271-1281.

44. Boer VO, Siero JC, Hoogduin H, van Gorp JS, Luijten PR, Klomp DW. High-field MRS of the human brain at short TE and TR. *NMR Biomed.* 2011;24(9):1081-1088.

45. Heckova E, Považan M, Strasser B, et al. Effects of different macromolecular models on reproducibility of FID-MRSI at 7T. *Magn Reson Med.* 2020;83(1):12-21.

46. Balchandani P, Spielman D. Fat suppression for 1H MRSI at 7T using spectrally selective adiabatic inversion recovery. *Magn Reson Med.* 2008;59(5):980-988.

47. Henning A, Fuchs A, Murdoch JB, Boesiger P. Slice-selective FID acquisition, localized by outer volume suppression (FIDLOVS) for 1H-MRSI of the human brain at 7 T with minimal signal loss. *NMR Biomed.* 2009;22(7):683-696.

48. Boer VO, Klomp DW, Juchem C, Luijten PR, de Graaf RA. Multislice ^{1}H MRSI of the human brain at 7 T using dynamic B_0 and B_1 shimming. *Magn Reson Med.* 2012;68(3):662-670.

49. Pan JW, Lo KM, Hetherington HP. Role of very high order and degree B_0 shimming for spectroscopic imaging of the human brain at 7 tesla. *Magn Reson Med.* 2012;68(4):1007-1017.

SUPPORTING INFORMATION

Additional supporting information may be found online in the Supporting Information section at the end of this article.